

Modeling the topography of shallow braided rivers using Structure-from-Motion photogrammetry



L. Javernick^{a,*}, J. Brasington^b, B. Caruso^a

^a Department of Civil and Natural Resources Engineering, University of Canterbury, Private Bag 4800, Christchurch 8140, New Zealand

^b School of Geography, Queen Mary, University of London, London E1 4NS, United Kingdom

ARTICLE INFO

Article history:

Received 1 September 2013

Received in revised form 3 January 2014

Accepted 10 January 2014

Available online 21 January 2014

Keywords:

Fluvial modeling

DEM

SfM

PhotoScan

Photogrammetry

Point cloud filtering

ABSTRACT

Recent advances in computer vision and image analysis have led to the development of a novel, fully automated photogrammetric method to generate dense 3d point cloud data. This approach, termed Structure-from-Motion or SfM, requires only limited ground-control and is ideally suited to imagery obtained from low-cost, non-metric cameras acquired either at close-range or using aerial platforms. Terrain models generated using SfM have begun to emerge recently and with a growing spectrum of software now available, there is an urgent need to provide a robust quality assessment of the data products generated using standard field and computational workflows.

To address this demand, we present a detailed error analysis of sub-meter resolution terrain models of two contiguous reaches (1.6 and 1.7 km long) of the braided Ahuriri River, New Zealand, generated using SfM. A six stage methodology is described, involving: i) hand-held image acquisition from an aerial platform, ii) 3d point cloud extraction modeling using Agisoft PhotoScan, iii) georeferencing on a redundant network of GPS-surveyed ground-control points, iv) point cloud filtering to reduce computational demand as well as reduce vegetation noise, v) optical bathymetric modeling of inundated areas; and vi) data fusion and surface modeling to generate sub-meter raster terrain models. Bootstrapped geo-registration as well as extensive distributed GPS and sonar-based bathymetric check-data were used to quantify the quality of the models generated after each processing step.

The results obtained provide the first quantified analysis of SfM applied to model the complex terrain of a braided river. Results indicate that geo-registration errors of 0.04 m (planar) and 0.10 m (elevation) and vertical surface errors of 0.10 m in non-vegetation areas can be achieved from a dataset of photographs taken at 600 m and 800 m above the ground level. These encouraging results suggest that this low-cost, logistically simple method can deliver high quality terrain datasets competitive with those obtained with significantly more expensive laser scanning, and suitable for geomorphic change detection and hydrodynamic modeling.

© 2014 Elsevier B.V. All rights reserved.

1. Introduction

During the past decade, advances in survey and sensor technology have created new opportunities to investigate the structure and dynamics of fluvial systems through the development and differencing of high quality digital terrain models for change detection (Wheaton et al., 2010; Brasington et al., 2012) and hydrodynamic numerical model boundary conditions (Williams et al., 2013a). These advances have been delivered through the advent of digital ground-survey technologies, in particular the Global Positioning System (GPS) (Brasington et al., 2000; Wheaton et al., 2013) and perhaps more fundamentally through the emergence of remote survey methods, including softcopy photogrammetry (Lane et al., 2000; Westaway et al., 2003), aerial light detection and ranging (LiDAR) (Charlton et al., 2003; Hilldale and Raff, 2008) and terrestrial laser scanning (TLS) (Brasington et al., 2012; Williams et al., 2013b).

The adoption of these geomatic technologies has driven a profound increase in the dimensionality of topographic datasets and used within river science, and geomorphology more broadly. Traditional cross-section models have been replaced by 2.5-dimensional (2.5d) digital elevation models (DEMs), and more recently by fully 3d point clouds and surface models (Kreylos et al., 2013). However, fluvial terrain modeling remains challenging due to complex topography, partial inundation, and high sediment mobility. These challenges are particularly true for braided rivers and are compounded with large study sites. While the revolutionary power of these geomatic advances has been utilized to develop quality fluvial terrain models, the high hardware and facility costs, and/or labor intensive and lengthy data acquisition limit the extent and frequency of surveys.

Advances in computer vision and image analysis have led to the development of a novel photogrammetric approach called Structure-from-Motion (SfM) that when coupled with Multi-View Stereo (MVS) offers a fully automated method capable of producing high resolution DEMs with low cost consumer grade cameras (Agisoft, 2010; Fonstad et al., 2013). Traditional photogrammetric DEMs were typically less

* Corresponding author. Tel.: +64 212465897.

E-mail address: luke.javernick@pg.canterbury.ac.nz (L. Javernick).

accurate and precise than airborne LiDAR (Baltsavias, 1999); however, SfM–MVS has produced terrain models with centimeter precision and point cloud resolutions that fall between LiDAR and TLS (Doneus et al., 2011; Fonstad et al., 2013) and has been utilized to accurately model objects on the centimeter to kilometer scale (James and Robson, 2012; Westoby et al., 2012). Recent studies have highlighted the convenience of SfM–MVS by utilizing unmanned or ultralight aircraft (James and Robson, 2012; Dandois and Ellis, 2013) as well as the potential time savings terrestrial image acquisition has over transporting heavy and bulky TLS equipment (James and Robson, 2012).

This paper presents a workflow production combining SfM–MVS, optical-bathymetric mapping, and point cloud filtering that produced three fluvial terrain models of the braided Ahuriri River, New Zealand with 0.5 m resolution and minimal vegetation noise. This workflow offers non-experts a method to produce quality fluvial terrain models with minimal data acquisition costs and moderate (initial surveys) to minimal (repeat surveys) field labor. In contrast to previous studies, this paper provides a rigorous quality assessment of the SfM–MVS performance measured against extensive real time kinematic (RTK)-GPS ground check-datasets for a 102 ha study-reach. To demonstrate the capabilities and limitations of such methods, these methods were extended to evaluate i) a 104 ha contiguous river reach that was comprised of limited quantity and quality geo-control and ii) a 206 ha river reach that was comprised of the two contiguous river reaches' datasets.

1.1. Structure-from-Motion and Multi-View Stereo

Several SfM software packages are currently available. Many, like Microsoft's PhotoSynth, are internet based and allow the user to load images via the internet and process the data remotely without parameter specification. PC based programs such as SFMToolkit and Agisoft's PhotoScan allow the user to set numerous parameters. While it is recognized that PhotoSynth and SFMToolkit are both capable of producing quality DEMs (e.g. James and Robson, 2012; Westoby et al., 2012), this research utilized PhotoScan (version 0.9.0) due to parameter control, user-friendly graphical user interface, inclusive transformation ability, and in part based on the exceptional results published in Doneus et al. (2011).

SfM–MVS generated point clouds are produced in three stages. During the first stage, SfM utilizes supplied photographs and tracking algorithms to identify, match, and monitor the movement of unique features (Verhoeven, 2011; Agisoft, 2012). Many SfM packages use the Scale Invariant Feature Transform (SIFT) object recognition system (Lowe, 2004) for this process; however, PhotoScan claims to achieve higher alignment quality using custom algorithms that are similar to SIFT (Semyonov, 2011). The second stage determines the camera's intrinsic (focal length, principal point, and lens distortion) and extrinsic (projection center location and the six exterior orientation parameters that define the image) orientation parameters by determining the optimal camera positions through greedy algorithms, and later improves their positions with a bundle-adjustment algorithm (Robertson and Cipolla, 2009; Semyonov, 2011; Verhoeven et al., 2012). In contrast to traditional photogrammetry, SfM does not require the 3d location and orientation of the camera at image capture, nor the 3d location of the control points to be known prior to scene reconstruction (Verhoeven et al., 2012; Westoby et al., 2012). Following the completion of the first two stages, a sparse point cloud has been generated as well as the location and position of every supplied image.

The third stage utilizes the previously determined intrinsic and extrinsic camera locations, a dense multi-view stereo reconstruction (DMVR), and every pixel of the provided images to produce a dense point cloud and a dense surface reconstruction referred to as a *mesh* (Agisoft, 2012). The resulting dense point cloud is generated in an arbitrary coordinate system; however, PhotoScan can transform the model into the absolute coordinate system provided that a minimum of three ground control points (GCPs) or camera coordinates has been recorded.

Transformation through the use of GCPs can be accomplished in the user-interface by manually identifying and marking the GCP object within the imported photographs. Once GCP identification has been completed and the corresponding xyz coordinates have been entered, a linear similarity transformation using seven parameters (three translation, three rotation, and one scaling) is automatically performed. Further, an *optimization* transformation method is also available which utilizes the modeled point cloud and camera parameters to reduce the difference between the model and supplied coordinates (Agisoft, 2012). However, PhotoScan's transformation algorithms are not fully disclosed and the final resulting point cloud may require user editing due to vegetation and/or additional noise.

1.2. Optical bathymetric mapping

Consistent with other photogrammetric studies, fluvial terrain models generated with SfM–MVS struggle to identify the inundated river bed elevation and thus a significant portion of the terrain remains undocumented. This is unacceptable for most fluvial terrain models due to the river beds' highly active geomorphology (Williams et al., 2011). However, many methods are available to acquire this bathymetric data including remote sensing methods such as bathymetric LiDAR and optical remote sensing (Westaway et al., 2003; Carbonneau et al., 2006; Wedding et al., 2008) as well as field data collection methods using radar, sonar, and RTK-GPS surveys (Brasington et al., 2003; Fonstad and Marcus, 2005; Williams et al., 2011). However, LiDAR methods are expensive and extensive field data collection can be an overwhelming task for large river studies. Thus, optical bathymetric mapping is a practical method to model the river bed elevation at sub-meter resolution (Marcus and Fonstad, 2008; Williams et al., 2011).

Optical bathymetric mapping requires a correlation between the water's depth and the water's color (Winterbottom and Gilvear, 1997) and works well for shallow water depth and minimal turbidity. To develop a river bed map of the inundated areas, three general steps are taken. First, to develop a relationship between the water's depth and the water's color, near-concurrent aerial photographs and water depth data are assessed. Second, a model of the water surface must be generated. Third, the spatial depth data are subtracted from the corresponding water surface elevation to develop the river bed elevation map. Given that SfM–MVS and optical bathymetric mapping require similar datasets, coupling the two methods to produce a fluvial terrain model is a convenient workflow.

2. Methods

2.1. Workflow

The workflow presented in this paper utilized PhotoScan's SfM–DMVR to generate the terrain surface for dry areas, the geospatial Topographic Point Cloud Analysis Toolkit (ToPCAT; Brasington et al., 2012) to reduce the point cloud resolution to i) improve data handling, and ii) to reduce vegetation noise, and finally optical-empirical bathymetric mapping to model the inundated terrain. The full production (Fig. 1) starts with the acquired aerial photographs, which were utilized in two ways. First, the photographs were uploaded into PhotoScan to produce a georeferenced SfM–DMVR point cloud that was then: i) decimated to reduce the point cloud resolution to a computationally manageable size as well as reduce vegetation noise, ii) utilized to model the dry surface terrain, and iii) used to derive the water surface elevation of the inundated areas. Secondly, PhotoScan utilized the upload photographs to produce mosaicked orthophotos which were: i) utilized with bathymetric data to develop an empirical-optical depth formula, ii) subtract the depth formula from the modeled water surface to obtain a river bed elevation model, and iii) discretize the model into a similar resolution as the SfM point cloud. Finally, the dry and wet point clouds were fused into one point cloud which was utilized to develop the digital elevation model.

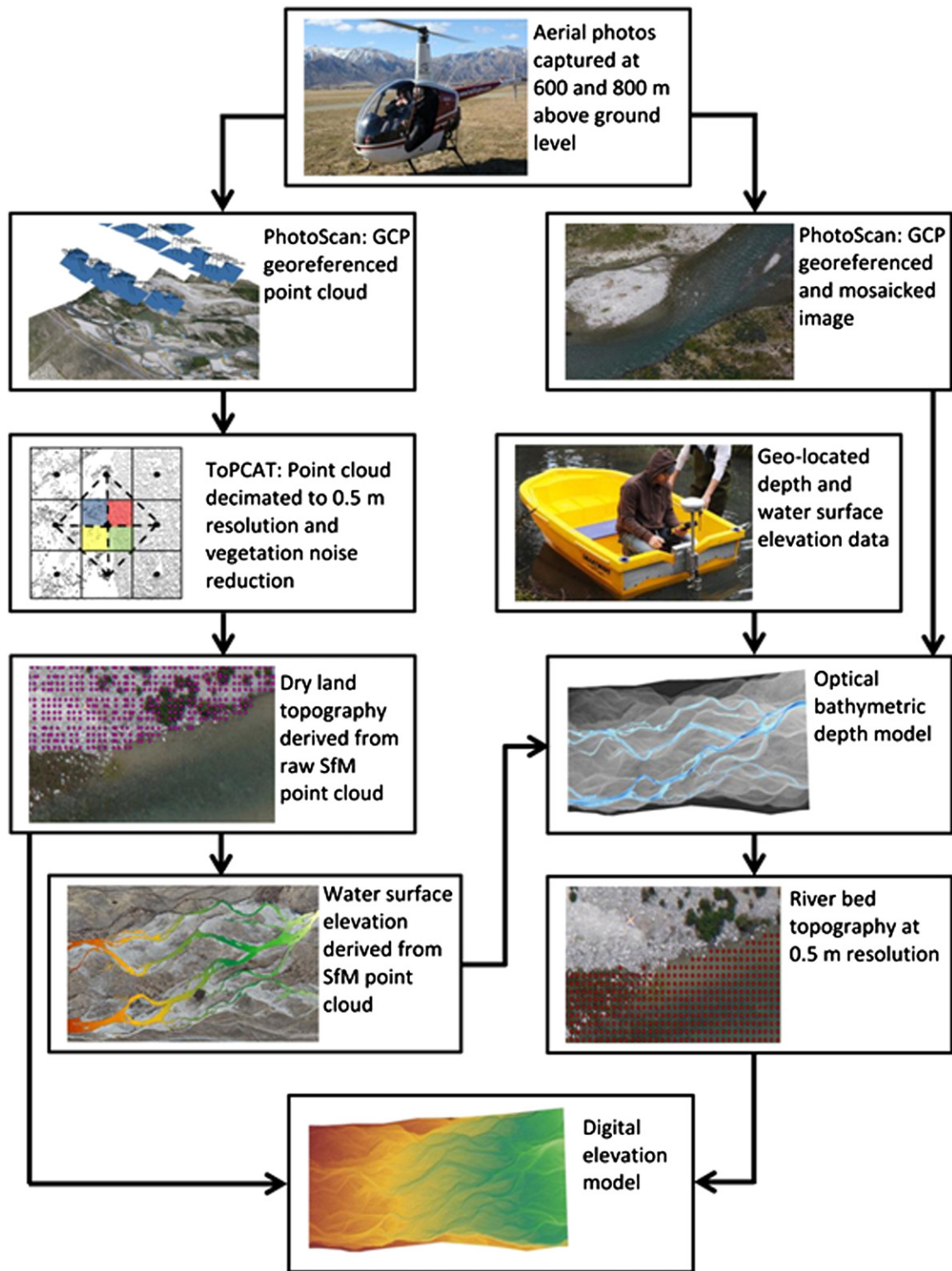


Fig. 1. Workflow illustration for fluvial terrain model production.

2.2. Study site

The braided Ahuriri River is located in the Southern Alps of the South Island, New Zealand and offered a challenging study site to test the terrain modeling workflow due to the complex floodplain topography, partial inundation, high sediment mobility, and moderate vegetation. With a drainage basin of 566 km² and annual

precipitation of 1775 mm, the Ahuriri River flows 70 km before draining into the artificial Lake Benmore (Hicks et al., 2011). Located 22 km upstream from Lake Benmore, the main *study reach* (Fig. 2) comprises an area of 1.6 × 0.65 km and has an average gradient of 0.9%. Surface grain diameter's ranges between $D_{25} = 14$ mm and $D_{100} = 256$ mm with D_{50} (median) = 30 mm, and subaqueous grain diameter's ranging between $D_{25} 8$ mm and $D_{100} 256$ with a

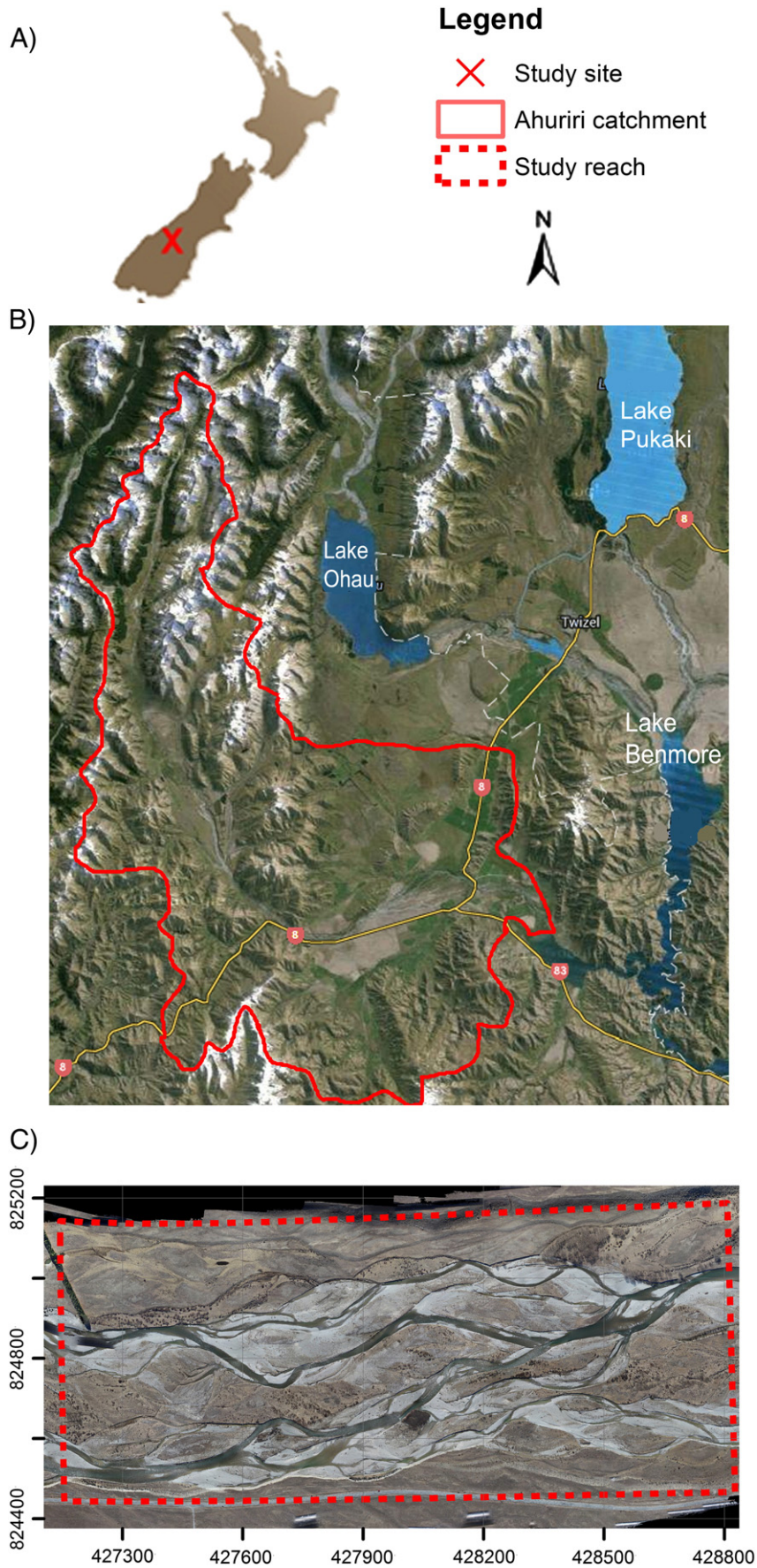


Fig. 2. Location maps. A) study site location in New Zealand. B) Ahuriri catchment. C) Study reach extent. Grid in NZGD 2000, Lindis Peak Circuit 2000 with X-axis Easting (m) and Y-axis Northing (m).

median grain diameter of 28 mm. Additionally, high tectonic activity occurs throughout the Southern Alps with present-day uplifting estimated up to 5 mm year^{-1} (Beavan et al., 2010). Together, these geological properties and moderate precipitation provide the Ahuriri River with an abundant sediment supply of coarse schist and greywacke (Land Information New Zealand, 2002). While sediment studies are scarce for the Ahuriri River, it has been estimated to yield 43,000 tonnes annually and modeled to yield 127,400 tonnes of suspended sediment annually (Griffits, 1981; as cited by Pickrill and Irwin, 1986; Hicks et al., 2011). Floodplain vegetation consists of both native and exotic species; however, the greatest density within the study reach includes herbaceous Russell lupins, matagouri and rosehip shrubs, and thickets of young and mature willow trees. Flow data has been recorded 8 km upstream of the study reach since 1963 and a hydrological assessment determined the river's mean flow of $23.4 \text{ m}^3 \text{ s}^{-1}$ and mean annual flood of $222 \text{ m}^3 \text{ s}^{-1}$.

2.3. Data collection

Field work was conducted during the austral winter of 2011 to ensure low river levels and sparse, dormant vegetation. While quality SfM-DMVR point clouds can be generated using oblique terrestrial photographs, the large scale study reach would have required multi-day data acquisition, and the moderate floodplain vegetation would have caused significant point cloud noise. Therefore, it was determined that near vertical aerial photographs would be acquired by hand from a manned Robinson R22 helicopter. This method allowed for fast (sub-hour) image capture covering the entire study reach and for a high grade digital camera which would have been too heavy for most UAVs. Flight planning determined the Canon 10.1 megapixel digital single lens reflex camera set at a 28 mm focal length (adjustable focal lens 18–55 mm) would result in minimal image distortion (near 35 mm equivalent) and would produce a target image object space resolution of 0.12 m when captured at 600 m above the ground level (AGL). To ensure adequate image overlap, flight speed was held at approximately 40 km h^{-1} ; pictures were taken at approximately three second intervals; and flight paths were segmented into four overlapping strips

parallel with the river's floodplain. This provided image side overlap of $\geq 60\%$ and top-bottom overlap of $\geq 70\%$. This procedure was repeated at 800 m AGL (0.16 m resolution) to ensure adequate image coverage.

Prior to taking aerial photographs, 95 GCPs were distributed throughout the study reach in a 100 m grid for georeferencing purposes (Fig. 3A). Each GCP was made of black polythene squares approximately $1.3 \times 1.3 \text{ m}$ with a superimposed cross made of yellow plastic strips 0.2 m wide; target centroids were surveyed using Trimble R8 GNSS system, operating RTK mode. All points were acquired in WGS84 and transformed into New Zealand national mapping coordinate system NZGD, Lindis Peak Circuit 2000. Given the relatively coarse object-space pixel resolution of the imagery, survey observations were acquired on a handheld rod with a pointed tip, and solutions obtained after five epochs with 3d point quality ranging between 2 and 5 cm in xyz (Trimble, 2012). In order to assess the quality of the DEM generated, 10,622 distributed RTK-GPS ground truth points were collected with the same methods and quality as previously stated (Fig. 3B). Similar to traditional photogrammetry limitations discussed by Chandler (1999) and Lane et al. (2000), SfM models produced from aerial images may represent the vegetation tops rather than the desired ground surface. Therefore, to fully evaluate the SfM performance, the ground truth data were split into three sets: i) a dataset utilizing all terrestrial points (except areas inundated with water), ii) a dataset edited to exclude areas of tall vegetation, steep slopes, and water, and iii) a dataset limited to vegetated areas. These three datasets will be referred to as *all ground truth*, *bare ground truth*, and *vegetation ground truth*, respectively.

Bathymetric surveying was conducted immediately following aerial photography. To provide geo-located water surface and depth measurements, a custom fabricated aluminum apparatus mounted the Trimble RTK-GPS R8 receiver directly above a Trittech PA500 altimeter (echo-sounder). Further, the echo-sounder was connected to the Trimble (TSC2) controller and recorded the sounder's National Marine Electronics Association (NMEA) data string output with the synchronized GPS coordinates at one hertz. In order to capture a large dataset, the apparatus, GPS and echo-sounder were attached to a small dinghy. Using a set of ropes, two individuals on opposite river banks navigated the dinghy down the river in a zigzag pattern (Fig. 3C). Due to the echo-sounder's requirement to sit 0.1 m below

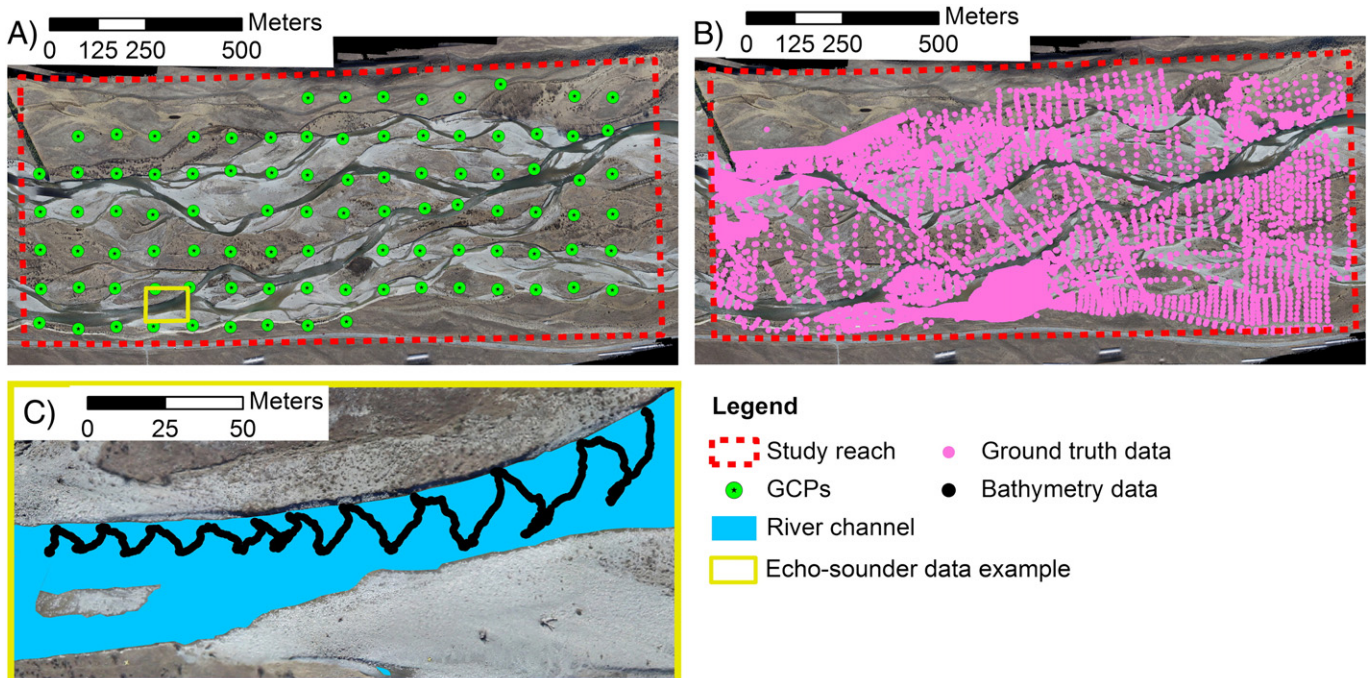


Fig. 3. Field data collection in the study reach. A) GCP distribution. B) All ground truth distribution. C) Example of echo-sounder data acquisition in main channel.

the water surface, it was not possible to record the depths in shallow water (<20 cm); thus, limiting the echo-sounder to the main river channel. Therefore, additional manual GPS depth measurements were collected in anabranches by recording the water surface elevation and wading into the river perpendicular to flow. In total, 6935 water depth points and 6931 water surface points were acquired.

2.4. Surface modeling and point cloud filtering

2.4.1. Surface modeling

Throughout this paper, the computer utilized consisted of: Intel CORE i7 (2600 @ 3.4 GHz, single CPU), 16 GB ram, a Gigabyte GTX 560Ti graphics card, and a 120 GB Intel Solid-State drive 520 series utilized to improve reading and writing speed. PhotoScan's point cloud generation process offers users with little photogrammetry experience a method to develop quality terrain point clouds; however, there are numerous parameter settings throughout the SfM, DMVR, and transformation stages (AgiSoft, 2012). In order to gain insight into the parameter functions and sensitivity and to achieve the best possible performance, multiple preliminary parameter tests were conducted on approximately 10% of the available data (aerial photographs, GCPs, and ground truthing) and assessments were based on the corresponding residual errors. The methods and results of these tests will not be discussed in-depth, but the final parameter values determined were applied to all models and are listed in Table 1. While sensitivity testing is not a requirement, the authors of this paper recommend similar procedures be conducted to ensure accurate model generation.

Using the parameters of Table 1, final linear and optimized transformation models were generated using 147 photographs that contained both 600 and 800 m AGL images and produced point clouds of +23 million points and point spacing of 0.25 m were determined using ArcGIS. Due to the unknown transformation process, the authors of this paper felt that it was necessary to illustrate the internal camera calibration that takes place during the various transformation stages. This was done by examining PhotoScan's camera calibration window prior to linear transformation, post linear transformation, and post optimization. To assess the quality of the SfM-DMVR terrain model, two quality assessments were conducted. The first assessed PhotoScan's transformation accuracy. This was performed by utilizing approximately two-thirds of the GCPs with randomly selected locations during the transformation stage, with the remaining GCPs withheld to provide check data (Chandler, 1999). The second quality assessment examined the model's surface accuracy by comparing the SfM-generated surface and the +10,000 RTK-GPS ground truth points. This was performed in ArcGIS by importing the 2.5d point cloud and generating a surface by i) using a Delaunay constrained triangular irregular network (TIN) and ii) converting the TIN into a surface raster.

Table 1
PhotoScan final parameter settings.

Parameter	Setting
SfM parameters:	
Quality	High
Pair selection	Disabled
DMVR parameters:	
Reconstruction method	Height field – sharp
Target quality	High
Face count	30 million
Filter threshold	0
Hole threshold	0
Transformation parameters:	
Optimization	Selected
Camera Accuracy (m)	10
Marker accuracy (m)	0
Projection accuracy (pix)	0.001
Aspect	Selected
Skew	Selected
p1 & p2	Selected

Table 2
Residual errors for the linear transformed study reach model.

	Data	n	ME (m)	RMSE (m)	MAE (m)	SDE (m)	
GCPs	x	Utilized	65	0.04	0.19	0.14	0.19
		Withheld	30	0.04	0.20	0.15	0.20
	y	Utilized	65	−0.06	0.17	0.14	0.17
		Withheld	30	−0.04	0.19	0.16	0.19
	z	Utilized	65	0.40	2.00	1.52	1.97
		Withheld	30	0.46	1.96	1.53	1.93
Ground truth	z	Bare	1985	0.42	2.27	1.75	2.23
		Veg.	134	1.71	2.69	2.16	2.08
		All	10,622	0.58	2.41	1.93	2.34

2.4.2. Point cloud filtering

With the raw 0.25 m point spacing point clouds computationally demanding, ToPCAT was utilized to reduce the resolution (Brasington et al., 2012; Rychkov et al., 2012). ToPCAT can achieve an intelligent decimation by overlaying the point cloud with gridcells (at the user specified length and width) to sort and calculate statistics for the points within each gridcell. Calculated statistics of the contained points include the gridcell's maximum, minimum, and average elevation, as well as first and higher order moments. Following the work of Brasington et al. (2012), the minimum elevation was utilized to model the terrain surface; as it has the greatest chance to represent the surface within vegetated areas. In this project, ToPCAT was utilized to reduce the raw resolution to 0.5 m, which greatly reduced the processing time yet preserved topographic detail. Throughout the remaining article, this model will be referred to as *SfM + ToPCAT*.

Regardless of the initial ToPCAT resolution reduction, vegetation noise prevailed in the SfM + ToPCAT model in areas of large vegetation clusters. As discussed by Brasington et al. (2012), coarse resolution terrain models can undesirably smooth river banks and bar-top chutes; however, vegetated areas can also be affected. Therefore, to identify and remove vegetation noise from the final DEM yet preserve as much topographic detail as possible, ToPCAT and ArcGIS were utilized to generate and difference various surface rasters (similar to Westaway et al., 2003). This consisted of a five step process. First, the original SfM-DMVR raw point cloud was filtered in ToPCAT to produce decimated point clouds with 0.75, 1, 2, and 3 m point spacing. Second, these coarse point clouds were generated into surface rasters in ArcGIS. Third, the coarse surface rasters were individually differenced from the SfM + ToPCAT (0.5 m resolution) surface raster to generate new surface rasters that identified elevation differences. With greater topographic and vegetation details represented in the SfM + ToPCAT raster, positive elevation differences regularly identified vegetated areas. Therefore, areas with elevation differences ≥ 0.4 m were initially identified in ArcGIS by raster differencing, and mapped with polygons. The 0.4 m vegetation threshold was considered appropriate to identify the study reach's vegetation that mainly consisted of ≥ 3 m willows, ≥ 1 m shrubs, and ≥ 0.5 m tall dormant Russell lupins. Fourth, aided

Table 3
Residual errors for the optimized study reach model.

	Data	n	ME (m)	RMSE (m)	MAE (m)	SDE (m)	
GCPs	x	Utilized	65	0.00	0.02	0.01	0.02
		Withheld	30	0.00	0.05	0.03	0.05
	y	Utilized	65	0.00	0.02	0.01	0.02
		Withheld	30	0.00	0.04	0.04	0.04
	z	Utilized	65	0.00	0.03	0.02	0.03
		Withheld	30	0.04	0.22	0.13	0.22
Ground truth	z	Bare	1985	−0.07	0.17	0.14	0.16
		Veg.	134	0.41	0.78	0.50	0.67
		All	10,622	−0.03	0.23	0.16	0.23

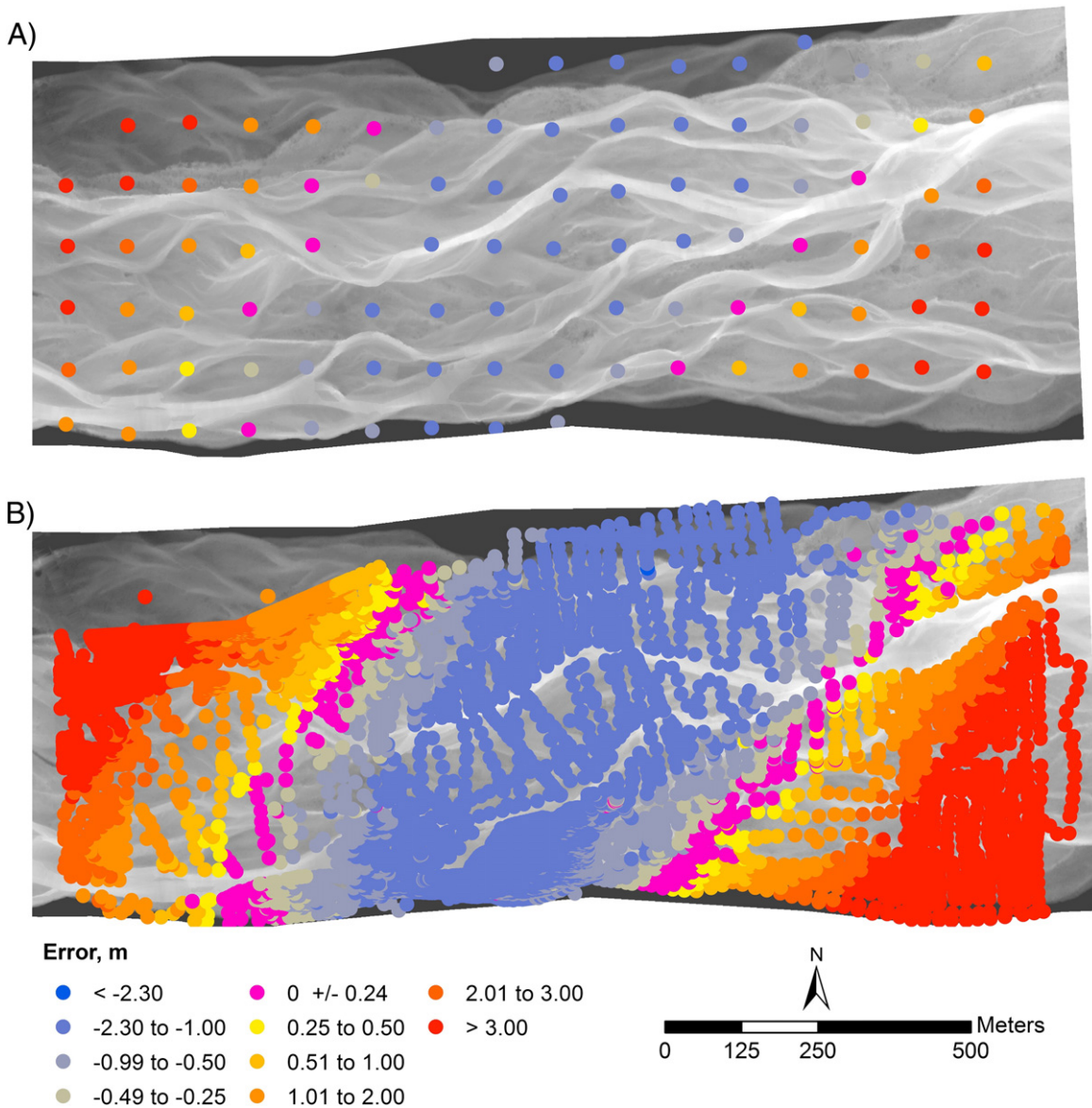


Fig. 4. Linearly transformed model's spatial distribution and color-coordinated residual z-errors for A) GCPs and B) all ground truth.

by aerial photographs, undesirably mapped areas such as river banks and steep slopes were excluded through minimal manual post-processing. Fifth, the remaining vegetated areas were removed from the SfM + ToPCAT point cloud and replaced with the coarse 3 m point cloud. Therefore, the final point cloud was a hybrid-resolution and will hereafter be referred to as *SfM-Veg*. To assess the effectiveness of ToPCAT vegetation removal, the three ground truth datasets (all, bare, and vegetation) were utilized to compare the accuracy of the SfM + ToPCAT model and the SfM-Veg model.

2.5. Bathymetric mapping

An optical-empirical bathymetric mapping method was utilized to model the river's depth, and was produced using the aerial photographs and depth measurements taken during the field work. This method is described by several previous studies (i.e. [Brasington et al., 2003](#); [Williams et al., 2011, 2013b](#)), and will not be discussed in great detail.

2.5.1. Water depth modeling

PhotoScan can produce orthophoto mosaicked images after model generation and transformation have been achieved. This study utilized

this method to produce mosaicked images of the study-site with default pixel size and average blending mode as it best produced a smooth transition between overlapping images and pixel brightness. This image was exported in TIFF format, and imported into ArcGIS where it was reduced to a 0.5 m resolution, cropped to the water extent, and the RGB band values were extracted to corresponding bathymetric data. Due to sunny conditions during image capture, images facing north had moderate sun glint. This caused poor results in original efforts to derive an empirical depth formula from a single mosaicked image. Therefore, the photographs were split into north- and south-facing sets, and separate mosaics were produced. Separately, the north or south images did not provide full coverage of the study reach's water extent; therefore, separate bathymetric models were generated and fused into one model.

Using a randomly selected subset of data that consisted of approximately two-thirds of the geo-located bathymetric depth data and corresponding RGB values, various band ratios were tested following the approach of [Williams et al. \(2013b\)](#). Least squares regression was used to determine the optimal empirical depth functions for both north and south image sets individually. Using the remaining one-third of the depth data the performance of the empirical depth formulas was assessed.

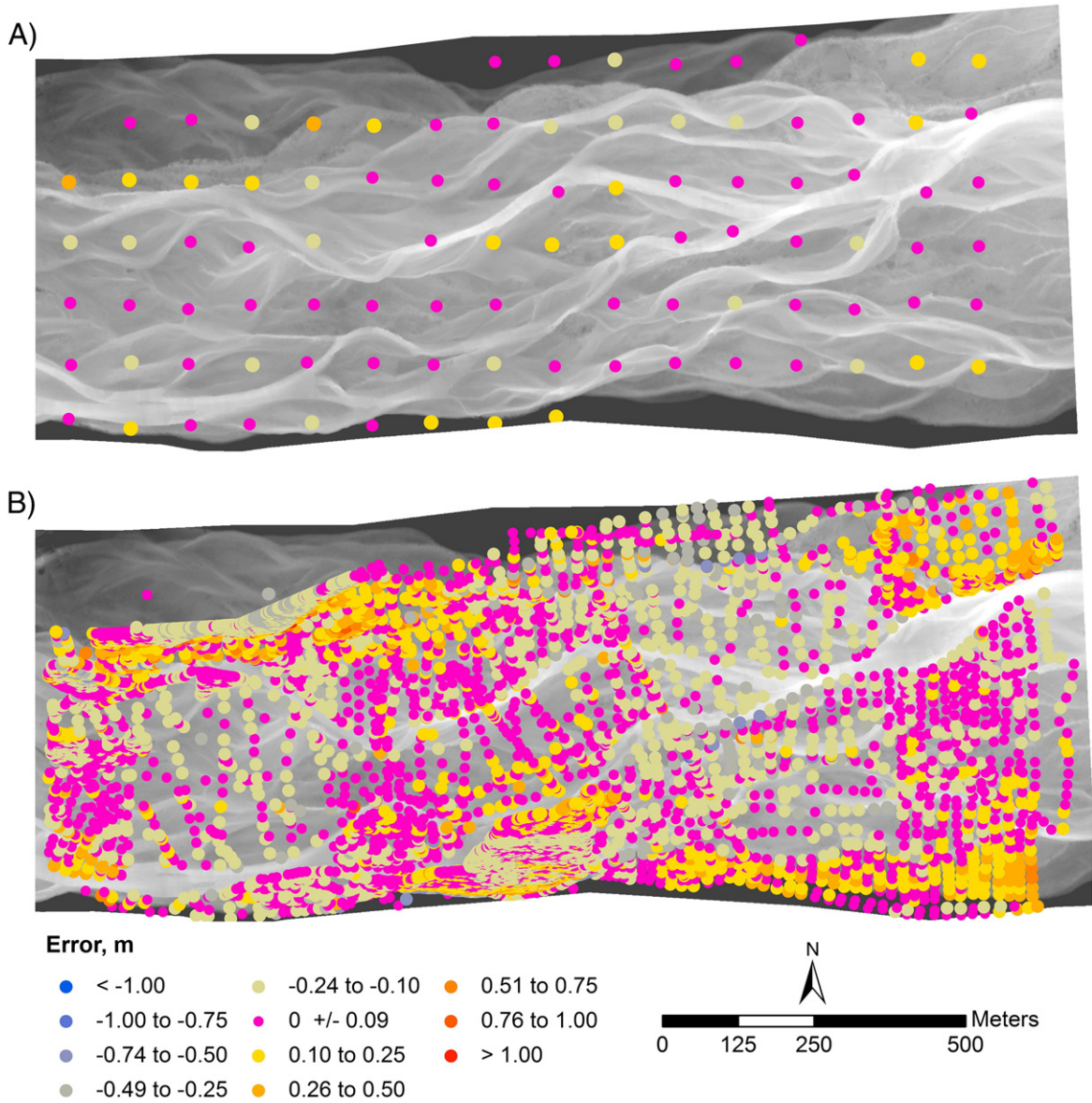


Fig. 5. Optimized transformed model's spatial distribution and color-coordinated residual z-errors for A) GCPs and B) all ground truth.

Table 4
PhotoScan calculated camera parameters during initial, linear, and optimization transformation.

Parameter	Initial	Linear	Optimized
<i>Focal length</i>			
<i>fx</i>	4896.87	4823.81	4812.29
<i>fy</i>	4869.87	4823.81	4813.94
<i>Principle point coordinates</i>			
<i>cx</i>	1944.00	1966.23	1966.57
<i>cy</i>	1296.00	1384.03	1390.76
Skew	0.00	0.00	11.05
<i>Radial distortion</i>			
<i>k1</i>	0.00	-0.11	-0.09
<i>k2</i>	0.00	0.25	0.12
<i>k3</i>	0.00	-0.27	0.08
<i>Tangential distortion</i>			
<i>p1</i>	0.00	0.00	-0.0002
<i>p2</i>	0.00	0.00	-0.0001

2.5.2. Water surface modeling

In order to utilize the depth formula to model the river bed elevation, the water surface elevation was required. Therefore, the water surface was modeled by utilizing the SfM-Veg point cloud along the water's edge, and interpolating a TIN surface across the river channels (similar to the methods of Brasington et al., 2003; Westaway et al., 2003; Williams et al., 2011). Minor editing was performed in areas of river bends with steep

Table 5
Ground truth residual errors for the SfM-Veg model.

	ME (m)	RMSE (m)	MAE (m)	SDE (m)
<i>Study reach</i>				
Bare	-0.07	0.17	0.14	0.16
Veg.	0.21	0.40	0.34	0.35
All	-0.04	0.20	0.16	0.20

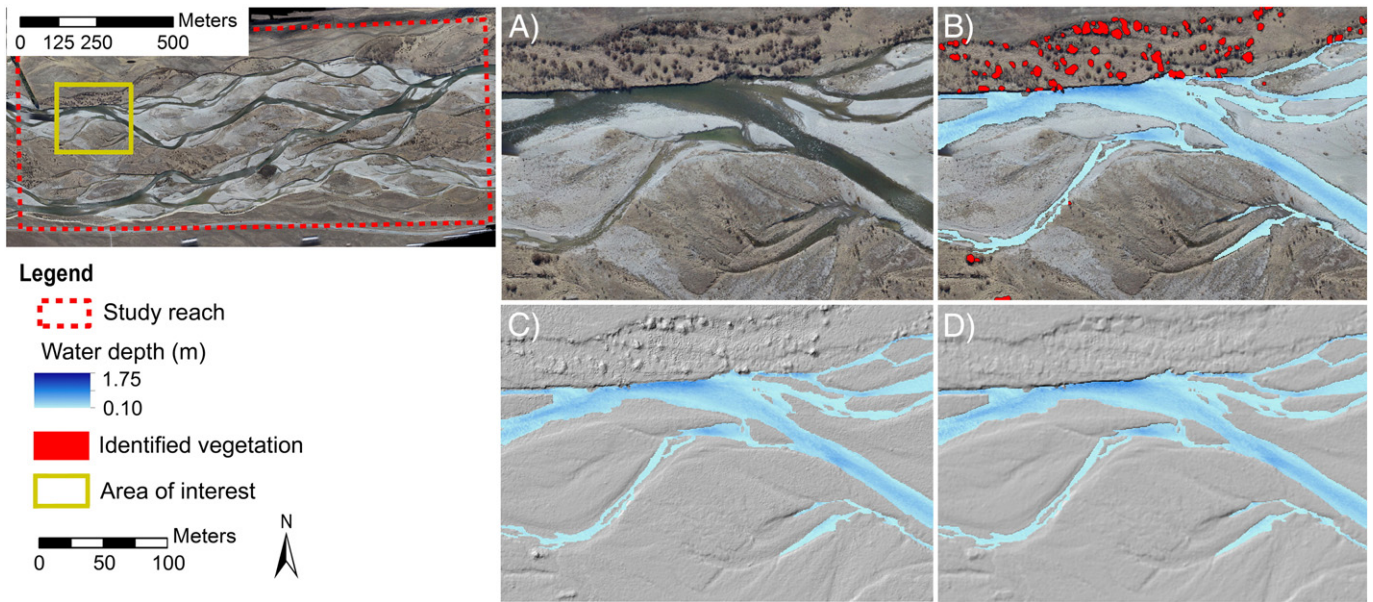


Fig. 6. ToPCAT vegetation noise reduction. A) example area, B) vegetation identified using ≥ 0.4 m threshold, C) topographic detail of SfM + ToPCAT raster, and D) topographic detail of SfM-Veg raster.

banks (natural levee), and final assessment was performed using the water surface elevation recorded by the GPS equipped echosounder data.

The final river bed model was generated in ArcGIS by discretizing the water surface elevation raster into a 0.5 m resolution point cloud (matching the SfM-Veg resolution) and appending the corresponding

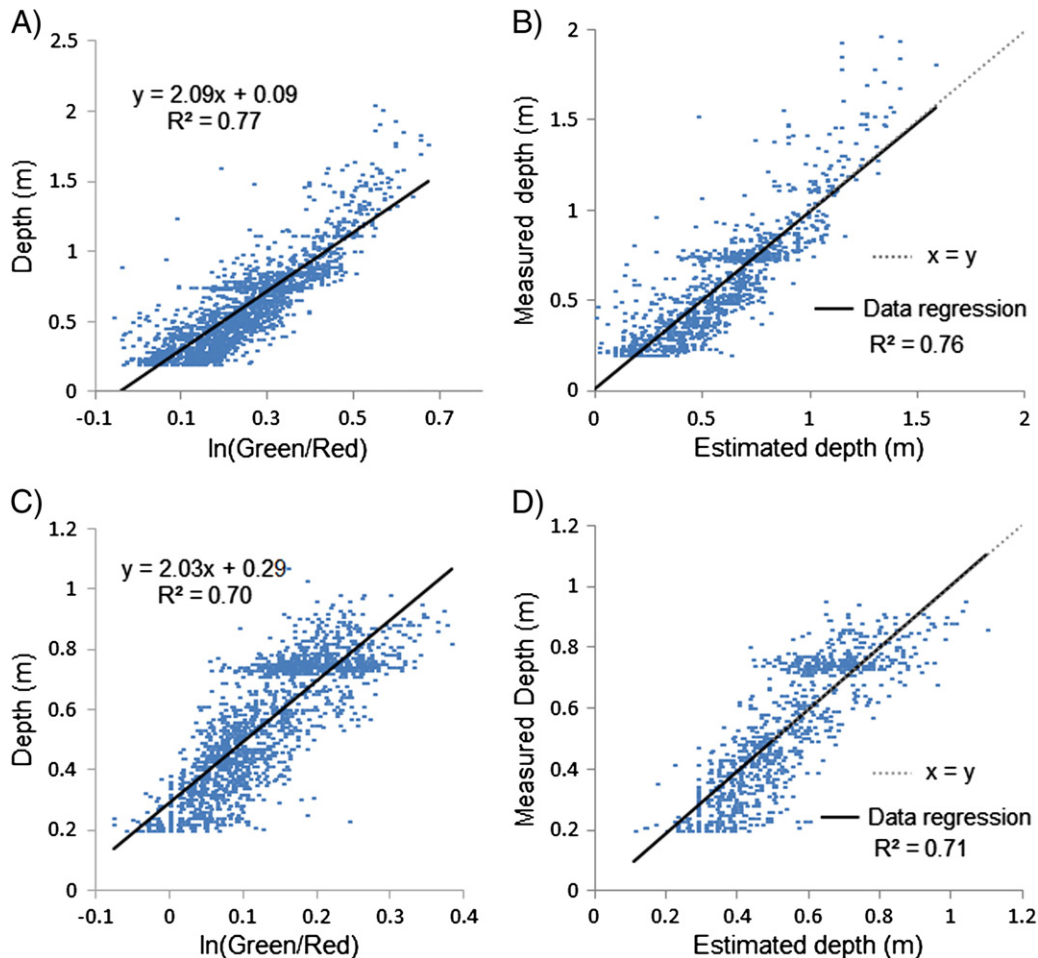


Fig. 7. Optical-empirical bathymetric results for: A) south-facing derived depth formula and relationship, B) south-facing model vs. measured results, C) north-facing derived depth formula and relationship, and D) north-facing model vs. measured results.

Table 6
Bathymetric mapping residual errors.

	<i>n</i>	<i>ME</i> (m)	<i>RMSE</i> (m)	<i>MAE</i> (m)	<i>SDE</i> (m)	Relative error (%)
Empirical depth						<i>MAE</i> /mean river depth
North facing	724	0.00	0.11	0.09	0.11	16.2
South facing	1376	−0.01	0.14	0.10	0.14	18.0
Water surface elevation						<i>MAE</i> / <i>2D</i> ₉₀
Combined model	6391	−0.05	0.18	0.15	0.18	72.8
River bed elevation						<i>MAE</i> / <i>2D</i> ₉₀
Combined model	6395	−0.06	0.31	0.27	0.31	131.1

RGB band values. Using the depth formula and RGB values, depths were calculated and subtracted from the water surface elevation; thus, providing the river bed elevation point cloud. Finally, the accuracy was

assessed using the river bed elevation recorded from the GPS equipped echo-sounder data.

2.6. DEM quality assessment

The final study reach DEM was produced by combining the SfM–Veg and bathymetric point clouds in ArcGIS, resampling a Delaunay TIN, and converted into a raster map. The quality assessments were as follows: i) SfM–DMVR georeferencing assessed from bootstrapping 30 GCPs for independent check data, ii) vertical topography assessment for exposed, vegetated, and all ground truth areas with dense GPS data, iii) bathymetric depth estimation by bootstrapped depth measurements, and finally iv) river bed elevation assessment following the incorporation of the water surface results. In the context of this paper, bootstrapping refers to the method of utilizing

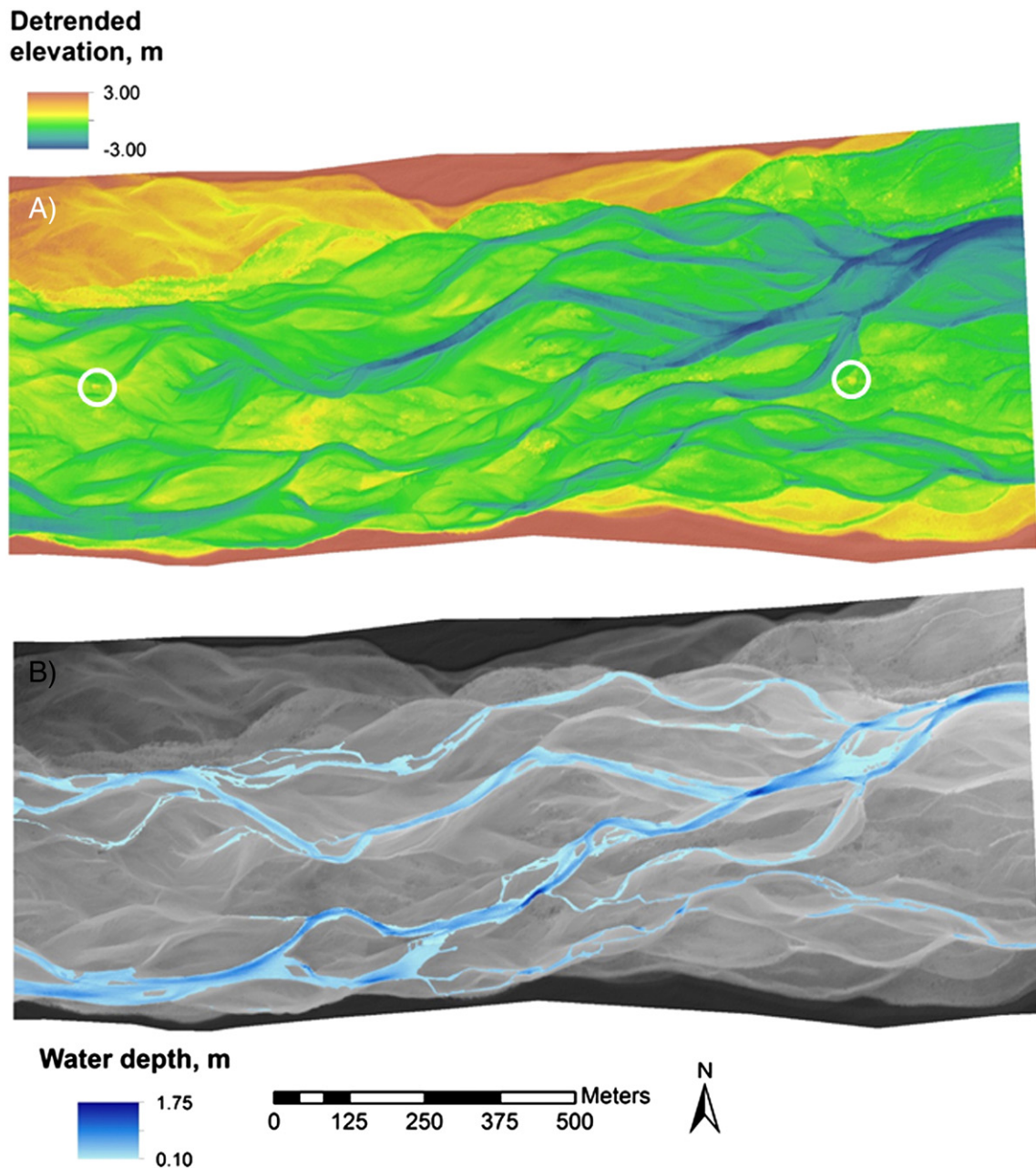


Fig. 8. Final A) detrended DEM, and B) bathymetric modeled water depth for the study reach.

Table 7
Fluvial terrain mapping error statistics for various geomatic technologies.

Survey technology	ME (m)	SDE (m)	Reference
Dry surface: Photogrammetry	0.084	0.26	Westaway et al. (2003)
Wet channel: Optical bathymetry	0.26	0.32	
Dry surface: LiDAR	0.21	0.07	Legleiter (2012)
Wet channel: Spectrally based bathymetry	0.24	0.15	
Dry surface: TLS	−0.02 to −0.06	0.007 to 0.029	Williams et al. (2013b)
Wet channel: Optical bathymetry	0.027	0.126	

approximately two-thirds of a dataset for model development, and withholding the remaining one-third to provide check data. GCP quality assessment was accomplished by utilizing PhotoScan's calculated residual errors which are produced by subtracting the models estimated values (xyz) from the user supplied GPS coordinates. Ground truthing was assessed by differencing the raster surface from the various surveyed GPS data. In both assessments, positive errors indicate that the model was above the surveyed surface. To evaluate the DEM quality, the residual errors were calculated and include root mean squared error (measure of surface quality, *RMSE*), the absolute mean error (measure of average non-directional height differences, *MAE*), the mean error (as a measure of accuracy, *ME*), and the standard deviation (as a measure of the precision, *SDE*) (Chandler, 1999; Lane et al., 2000).

$$RMSE = \sqrt{\frac{\sum_{i=1}^n (Est_i - Obs_i)^2}{n}} \quad (1)$$

$$SDE = \sqrt{\frac{\sum_{i=1}^n ((Est_i - Obs_i) - (\overline{Est_i} - \overline{Obs_i}))^2}{n}} \quad (2)$$

where Est_i is the SfM-DMVR determined elevation and Obs_i is the observed RTK-GPS elevation. In addition to these error assessments, relative error percentages were calculated for the water depth, water surface, and river bed elevations. The water depth relative error was calculated by dividing *MAE* by the mean river depth (0.55 m), and the water surface, and river bed elevation relative errors were calculated by dividing *MAE* by the surface roughness value of $2D_{90}$ (0.206 m). However, these assessments attempt to compare the modeled surface to discrete GPS and echo-sounder data that has inherent uncertainty (~0.02 m and 0.025% depth range, respectively) and additional sources of errors such as incorrect antenna height, un-level data collection, and blunders (Brasington et al., 2000, 2003). Nevertheless, the GPS and echo-sounder data provide an indication of the model's performance.

3. Results and discussion

3.1. SfM-DMVR

3.1.1. Georeference accuracy

Accuracy assessments for the SfM + ToPCAT-generated study reach models (linear transformation in Table 2 and optimized in Table 3) revealed that the optimized model had superior performance. The linear model results show that the utilized and withheld GCPs have *x*- and *y*-errors in the decimeter range; however, the *z*-errors were considerably higher. Spatially presenting these GCP *z*-errors (Fig. 4A) shows a distinct pattern of positive *z*-errors at the upstream and downstream ends and negative *z*-errors in the midsection. The optimized model's GCP errors revealed similar performance within the specific dimensions and with the withheld GCPs producing higher errors. The *x*- and *y*-dimensions residual errors showed high accuracy and precision; however, the *z*-errors

were considerably higher for the withheld GCPs. Spatially plotting the optimized GCP *z*-errors (Fig. 5A) revealed a random error distribution and suggests a successful transformation. Camera calibration parameter results are shown in Table 4 and illustrate the internal camera calibration during the various transformation stages. As shown, the skew and tangential distortion parameters are not adjusted from the initial to linear transformation, yet all parameters are slightly adjusted from the linear to optimized transformation stages.

3.1.2. Surface accuracy

Segmenting the GPS ground truth data into various categories provided: i) 10,622 points for all ground truth and provided an overall performance for the SfM in all areas, ii) 1985 points for the bare ground truth and provided a performance check for areas that were expected to perform well (i.e. bare areas without drastic vertical relief or vegetation), and iii) 134 points for the vegetation ground truth which were expected to perform poorly. Comparing the ground truth results of the linear (Table 2) and optimized (Table 3) models, the optimized transformed model's surface accuracy outperformed the linear model. Surface accuracy for the linear model showed consistent errors in the meter range. Conversely, the optimized models results were consistently in the decimeter range, including the less accurate vegetation ground truth areas. Finally, assessing the ground truth spatially plotted *z*-errors affirmed that the linear model (Fig. 4B) produced biased results and the optimized model (Fig. 5B) had considerably less error patterns; however, clusters of larger and smaller errors were present. While some *z*-errors were influenced by the surrounding vegetation, these areas consisted of only 134 points of the 10,622 plotted.

3.2. ToPCAT vegetation reduction

Applying the ToPCAT vegetation reduction method to the optimized SfM + ToPCAT model, approximately 1% of the point cloud was replaced with the 3 m resolution point cloud. Comparing the residual errors of the optimized SfM + ToPCAT model (Table 3) and optimized SfM-Veg model (Table 5) revealed that the vegetation reduction considerably improved the accuracy and precision of vegetated areas; however, the overall performance was still below the reach-wide SfM accuracy. Further assessment showed that the bare areas were unaffected, and all ground truth had a slight general improvement. A sample area of this process is illustrated (Fig. 6), and reveals noticeable vegetation noise reduction.

3.3. Bathymetry

Testing revealed that the natural log of the green-over-red band ratio achieved the strongest depth-band ratio relationship for both north- and south-facing datasets. Using this relationship, the corresponding empirical depth formulas were derived (Fig. 7a,c) and evaluation produced results with high accuracy and decimeter precision (Fig. 7b and d, and Table 6). The SfM-Veg derived water surface elevation model shows a slight negative biased accuracy and precision errors in the decimeter range, which are conveyed into the performance of the final river bed elevation model.

4. Discussion

4.1. Final DEM

The linear model results (Table 2) show a successful transformation for the *x*- and *y*-dimensions with errors in the decimeter range. However, the *z*-errors were an order of magnitude higher and would not suit the objectives of most fluvial terrain models. Further concern was raised with the spatial error curvature pattern shown in Fig. 4, which suggests that PhotoScan's linear transformation produces a spatial bias. Reviewing the camera calibration results of Table 4 and considering

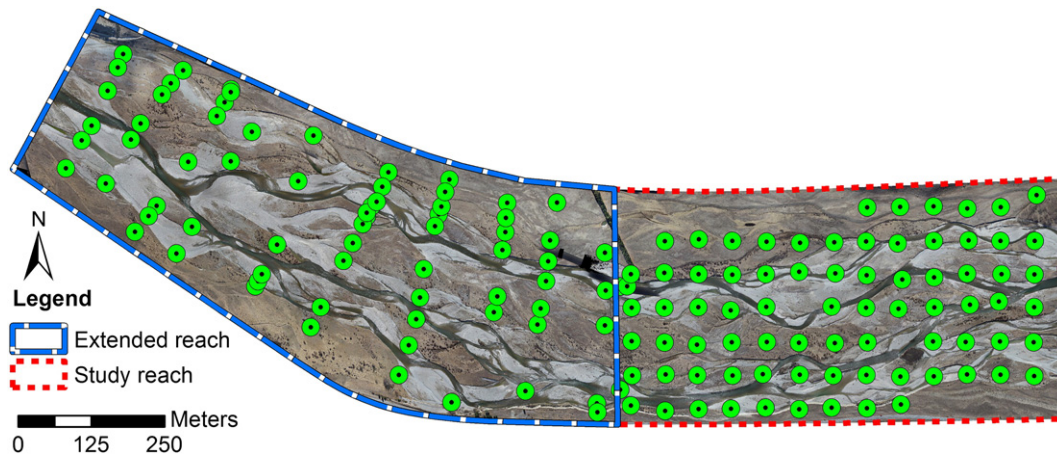


Fig. 9. Extended reach (upstream of the study reach extent) and the identified GCPs.

the superior results of the optimized model, it is questionable if image distortion and lack of lens distortion calibration caused such inaccuracies in the linear transformation model.

The optimized model's GCPs and ground truth (excluding vegetation) produced consistent results with errors in the decimeter range. Withheld and utilized GCP errors show that slight photocontrol dependence exists for accurate transformation for the x- and y-dimensions, and larger dependence for the z-dimension. Comparing the GCP z-errors with the bare and all ground truth z-errors revealed a similar performance. However, the ground truth mean errors became negative. This was likely caused by the use of the ToPCAT z-minimum data to represent the terrain. While a negative mean was undesirable, the overall accuracy impact of ToPCAT appears to be minimal when comparing the withheld GCP and ground truth residuals. Nevertheless, the results of the optimized model's GCPs and ground truth suggest a successful transformation with minimal systematic errors in the surface model. Reviewing the camera parameter values of Table 4, all parameters including the skew and tangential distortion were adjusted during the process from linear to optimized transformation which greatly improved the model's accuracy.

As illustrated by the vegetation ground truth data (Table 3), vegetated areas produce large inaccuracies in the SfM + ToPCAT model. However, the ToPCAT vegetation reduction method can drastically reduce the vegetation noise and slightly improved the overall model (Table 5). While the vegetation influence decreased by as much as 50%, the accuracy and precision of vegetated areas remained well below the reach-wide SfM performance. This was likely influenced by the utilized vegetation threshold value of 0.4 m. While identified vegetated areas were patched using the local z-minimum (3 × 3 m search window), the resulting elevation could contain inaccuracies just below this threshold. Further, it is possible that the point cloud failed to penetrate the vegetation's canopy, resulting in minimal noise reduction.

Table 8
Extended reach residual errors for SfM + ToPCAT model.

	Data	n	ME (m)	RMSE (m)	MAE (m)	SDE (m)	
<i>Extended reach</i>							
GCPs	x	Utilized	47	0.01	0.10	0.08	0.10
		Withheld	23	0.01	0.21	0.17	0.21
	y	Utilized	47	0.01	0.13	0.09	0.13
		Withheld	23	-0.01	0.13	0.09	0.13
z	Utilized	47	0.01	0.18	0.15	0.18	
		Withheld	23	0.13	0.36	0.28	0.34
	Ground truth	Bare	1116	-0.03	0.29	0.23	0.29
		Veg.	10	0.35	0.71	0.60	0.65
All		1233	0.05	0.27	0.24	0.27	

Therefore, these results may be improved by increasing the ToPCAT resolution reduction and/or lowering the vegetation threshold height. However, both of these practices would reduce the automation of this application by creating additional manual editing of non-vegetated areas.

The optical-empirical bathymetric mapping method utilized in this paper closely followed the methods utilized by Williams et al. (2013b); with the exception of splitting the mosaics into north- and south-facing images. As shown in Fig. 7, the south-facing mosaic depth to band ratio developed a higher R² than the north- (sun) facing mosaic, which was expected due to the sun interference. Comparing these results to Williams et al. (2013a) who achieved a depth to blue-over-red band ratio of R² = 0.806, the results presented in this paper were slightly less, but comparable (R² = 0.77 and 0.70). Considering that the water depth of this study reach rarely exceeded 1.5 m, the relative error results demonstrate the limitations of this method; however, these ME and SDE errors were comparable to the final SfM-Veg model's accuracy and precision. Further assessment revealed that the utilizing the SfM-Veg point cloud produced a water surface elevation model with similar errors as the bare ground truth data and the relative error below 100% indicated that the errors were less than that of the sediment size influence. The final river bed elevation combined the depth and water surface, and naturally the errors were conveyed to produce results with a negative mean error and residuals of +0.27 m. The relative errors of the river bed elevation were calculated over 100% and thus indicating that the errors are likely larger than the sediment grain size influence.

The final DEM raster was generated by combining the SfM-Veg and bathymetric point clouds. Linearly detrending this DEM to an origin of the water surface elevation offered a final visual inspection (Fig. 8) and revealed a smooth transition between the dry and wet areas, suggesting a successful data fusion. Two elevation spikes were identified (white circles), which were confirmed to be large vegetated areas (+140 m²) and were not detected nor removed by the ToPCAT vegetation reduction method. This was expected since ToPCAT vegetation smoothing resolution of 9 m² would not detect such large areas. However, given the moderate vegetation within this reach, results illustrate the

Table 9
Extended reach SfM-Veg ground truth residual errors.

	ME (m)	RMSE (m)	MAE (m)	SDE (m)
<i>Extended reach</i>				
Bare	-0.01	0.29	0.23	0.29
Veg.	0.10	0.56	0.43	0.59
All	0.03	0.29	0.22	0.29

potential and limitations of the SfM–Veg application. Finally, artifacts such as elevation steps visible by illuminated straight lines were not observed, suggesting that this model had adequate photograph overlap and quality. This also highlights PhotoScan’s ability to utilize photograph datasets taken at varying elevations, which has been problematic in past photogrammetric studies (e.g. Marzoff and Poesen, 2009). Finally, to provide context for this study’s results, Table 7 presents the results of other fluvial terrain models produced with various geomatic technologies. Comparing the results of Table 7 to the results of Tables 3 and 6 highlights the potential for SfM–MVS coupled with optical bathymetric mapping comparable to more expensive and labor intensive LiDAR- and TLS-derived terrain models.

5. Method extension 1

Directly upstream of the study reach, a contiguous 1.7 × 0.6 km extended reach was photographed and surveyed during the original data collection (Fig. 9). However, the extended reach data and ground control were not collected for SfM purposes; rather to provide the necessary topographic ‘runin’ data for numerical modeling purposes of the study reach. Data collection of the extended reach included aerial photographs captured at 600 m AGL and 10 survey transects that provided 1487 RTK-GPS points that were geo-coded to identify water extent. Using 106 images, the extended reach SfM model generated a point cloud of over 18 million points with an average point spacing of 0.21 m. To provide the necessary photocontrol, 70 GCPs were retrofitted using field and aerial photographs to identify the natural objects that were recorded as part of the transect data. The remaining unused transect points taken in dry areas (1233) were utilized as ground truth data. Bathymetric points included both manual collection within the transects (184 points), as well as a small portion of the downstream end collected using the GPS equipped echo-sounder data (562 points). Therefore, combined data sets provide 714 depth and river bed elevation points and 594 water surface points.

Applying the same workflow production of ToPCAT resolution reduction, ToPCAT vegetation noise reduction, and bathymetric mapping, the SfM + ToPCAT model’s quality is presented in Table 8, SfM–Veg quality in Table 9, and bathymetric mapping in Table 10. However, it should be recognized that the 10 transects do not provide an adequate ground truth distribution. Therefore, a full evaluation of the extended reach’s true performance was not possible.

The SfM + ToPCAT GCP results (Table 8) show that the optimized transformation performed well in areas of photocontrol, but had less accuracy in areas without, especially for the x- and z-dimensions. While this result was expected for the z-dimension, the x-dimension inaccuracy suggested poor horizontal GCP retrofitting. The bare and all ground truth errors showed that the model was relatively accurate with mean errors near zero; however, the SDE shows that the model’s precision was less than the study reach. As expected from the study reach results, the vegetation noise reduction results were effective (Table 9) and produce slightly improved results for all areas surveyed. Plotting the GCP and all ground truth errors (Fig. 10) revealed that the midsection’s transects start with negative errors on the southern bank and gradually increase as they transverse the floodplain toward the northern bank.

Table 10
Extended reach bathymetric residual errors.

	<i>n</i>	<i>ME</i> (m)	<i>RMSE</i> (m)	<i>MAE</i> (m)	<i>SDE</i> (m)	Relative error (%)
Empirical depth						<i>MAE</i> /mean river depth
North facing	464	0.04	0.13	0.12	0.15	21.6
South facing	250	0.03	0.13	0.10	0.12	18.0
Water surface elevation						<i>MAE</i> /2 <i>D</i> 90
Combined model	594	−0.03	0.28	0.23	0.28	111.7
River bed elevation						<i>MAE</i> /2 <i>D</i> 90
Combined model	714	0.01	0.42	0.35	0.41	169.9

However, the errors at the reach ends show less discernible patterns. With minimal bias transformation and surface model produced for the study reach optimized model, it is likely that the higher z-errors and midsection error pattern results of the extended reach were caused by the less accurate retrofitted GCPs.

Since the aerial photographs of the study reach and extended reach were captured at the same time, the previously derived optical bathymetric depth formulas (Fig. 7) were applied to the extended reach. Using the depth data, the formulas produced relatively accurate depths and precision in the decimeter range and low relative errors (Table 10). The SfM–Veg-interpolated water surface elevation accuracy and precision was consistent with the SfM point cloud performance, which combined with the depth formulas produced river bed elevation model with considerably higher residual errors and relative errors than the study reach.

The final extended reach detrended DEM and bathymetric mapping are presented in Fig. 11. Visual observation revealed that the SfM–bathymetric point cloud fusion produced a seamless transition of wet and dry areas; however, a few artifacts were visible. First, two lines are visible and outlined (black and white boxes). Investigated using PhotoScan’s 3d mesh, these lines were sudden steps in elevation approximately 1 m (black box) and 0.5 m in height (white box). Photographs utilized in the SfM generation of these areas were similar in

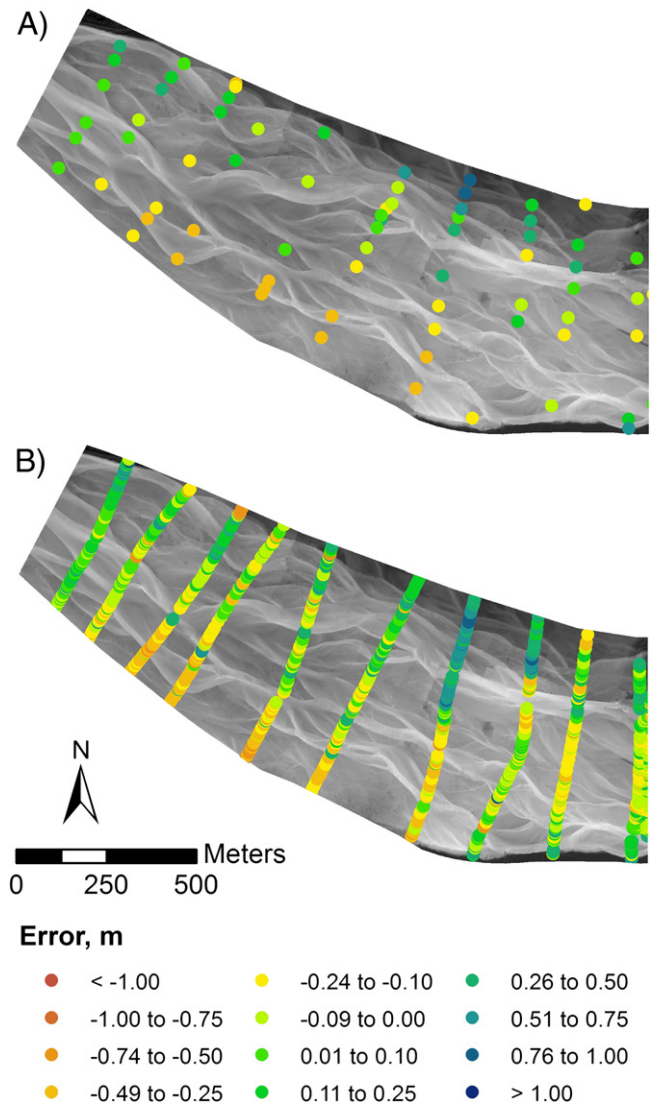


Fig. 10. Optimized transformed extended reach SfM + ToPCAT spatial distribution and color-coordinated residual z-errors for A) GCPs, and B) all ground truth points.

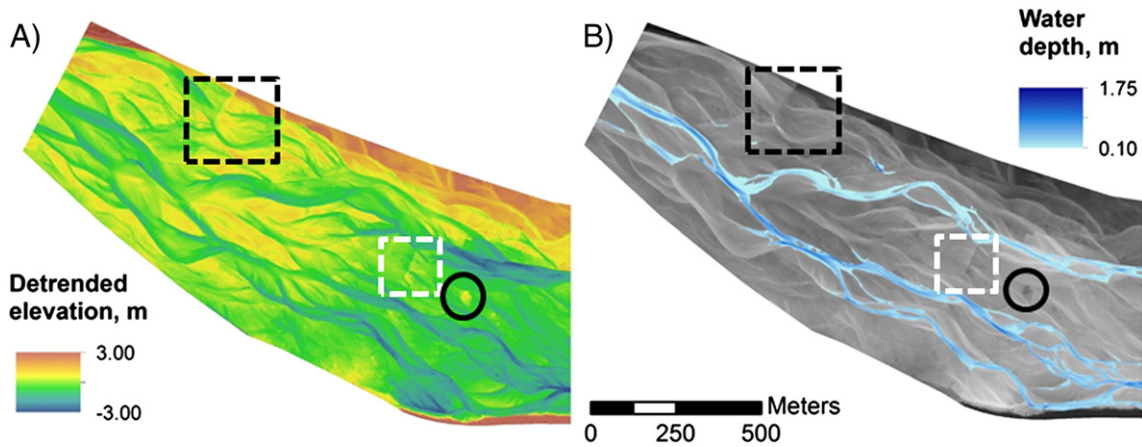


Fig. 11. Extended reach A) detrended DEM, and B) bathymetric modeled water depth.

quality and resolution, and captured at 600 m AGL; however, minimal overlapping photographs were available for these areas. The area identified in the white box was generated with three photographs, which was considerably less than the average of six. The area identified with the black box was generated with five photographs; however, image border alignment occurred for two of the photographs directly over the elevation step. Therefore, it appeared that the artifacts were produced by limited image data as well as the unfortunate chance of image border alignment. The second artifact identified was a visible spike in elevation (black circle). Investigation revealed a 480 m² (20 × 24 m) cluster of small willow trees that was not detected nor removed by the TopCAT vegetation reduction due to the large area.

6. Method extension 2

Combining the study reach and extended reach photographs (224 images captured at 600 and 800 m), a final optimized model was generated in PhotoScan that produced a point cloud of over 60 million points with an average point spacing of 0.23 m. This model was produced to provide a seamless DEM of the greater study site, and will be referred to as the *full reach*. Applying the terrain model workflow, the SfM + TopCAT results are presented in Table 11, the SfM–Veg results in Table 12, and the bathymetric model results in Table 13.

Table 11 Full reach SfM + TopCAT residual errors segmented into study reach and extended reach.

	Data	n	ME (m)	RMSE (m)	MAE (m)	SDE (m)	
<i>Study reach</i>							
GCPs	x	Utilized	65	0.00	0.06	0.03	0.06
		Withheld	30	0.00	0.05	0.03	0.05
	y	Utilized	65	0.00	0.05	0.03	0.05
		Withheld	30	0.01	0.05	0.04	0.05
z	Utilized	65	0.01	0.08	0.06	0.08	
		Withheld	30	0.03	0.13	0.10	0.13
	Ground truth	Bare	1,985	−0.05	0.13	0.10	0.12
		Veg.	134	0.41	0.69	0.52	0.53
All	10,622	−0.01	0.21	0.14	0.21		
<i>Extended reach</i>							
GCPs	x	Utilized	47	0.01	0.10	0.08	0.10
		Withheld	23	0.01	0.21	0.17	0.21
	y	Utilized	47	0.01	0.13	0.09	0.13
		Withheld	23	−0.01	0.13	0.09	0.13
z	Utilized	47	0.01	0.18	0.15	0.18	
		Withheld	23	0.13	0.36	0.28	0.34
	Ground truth	Bare	1116	−0.03	0.29	0.23	0.29
		Veg.	10	0.37	0.72	0.61	0.66
All	1233	0.05	0.27	0.24	0.27		

As expected from the previous results, the study reach outperformed the extended reach in every category. However, the study reach performance (Table 11) has significantly improved the GCP, bare ground truth, and all ground truth z-errors when compared to the study reach performance of Table 3. This was likely due to the added photocontrol of the extended reach, albeit less accurate. Conversely, the extended reach performance did not reciprocate this improvement. The vegetation reduction shows expected improvement in vegetated areas, with the overall errors lower than the previous results; likely improved by SfM model's accuracy. Spatially plotted GCP and all ground truth errors (Fig. 11) revealed the same performance of the previously discussed study reach and extended reach (Figs. 5 and 10).

The bathymetric model was produced using the same empirical depth formula described, and had similar results to the study and extended reach (Tables 6 and 10). However, noticeable improvement in the study reach's water surface elevation and river bed elevation accuracy, precision, and relative error occurred. Since these results were dependent on the SfM–Veg accuracy, the overall improvement was expected. Finally, evaluating the final detrended full reach DEM (Fig. 13) revealed that the previously identified elevation spikes and steps still occurred; however, no additional artifacts were identified. (See Fig. 12.)

7. Cost and convenience

Initial field data collection for the study reach was conducted in nine days. This included two days for GCP placement and geo-locating, one day for GCP retrieval, one day for bathymetric data collection, one hour flight time for aerial photograph collection, and five days for ground truth data collection. However, the acquired +10,000 ground truth points were excessive and could effectively be reduced to 4000. If systematically acquired, 4000 ground truth points (approximately 15 m spacing) would still provide adequate surface uncertainty for

Table 12 Full reach SfM–Veg ground truth residual errors.

	ME (m)	RMSE (m)	MAE (m)	SDE (m)
<i>Study reach</i>				
Bare	−0.05	0.13	0.10	0.12
Veg.	0.20	0.37	0.32	0.33
All	−0.02	0.18	0.13	0.18
<i>Extended reach</i>				
Bare	−0.03	0.29	0.23	0.29
Veg.	0.12	0.52	0.41	0.57
All	0.04	0.26	0.23	0.26

Table 13
Full reach bathymetric residual errors.

	<i>n</i>	<i>ME</i> (m)	<i>RMSE</i> (m)	<i>MAE</i> (m)	<i>SDE</i> (m)	Relative error (%)
<i>Study reach</i>						
Empirical depth						<i>MAE/mean river depth</i>
North facing	853	0.01	0.12	0.09	0.12	16.2
South facing	1,282	0.00	0.14	0.10	0.14	18.0
Water surface elevation						<i>MAE/2D₉₀</i>
Combined model	6421	−0.03	0.12	0.09	0.11	43.7
River bed elevation						<i>MAE/2D₉₀</i>
Combined model	5977	−0.02	0.26	0.20	0.25	97.1
<i>Extended reach</i>						
Empirical depth						<i>MAE/mean river depth</i>
North facing	81	0.04	0.13	0.12	0.15	21.6
South facing	115	0.03	0.13	0.10	0.12	18.0
Water surface elevation						<i>MAE/2D₉₀</i>
Combined model	594	−0.02	0.29	0.23	0.28	111.7
River bed elevation						<i>MAE/2D₉₀</i>
Combined model	590	0.01	0.43	0.35	0.41	169.9

propagated error DEM differencing (Wheaton et al., 2010; Wheaton, 2012). Therefore, to acquire the bathymetry data, field work could reasonably be completed in five days by one individual and a sixth day with two individuals. While the total field work may take several days, SfM coupled with aerial platforms can provide rapid topography acquisition. This is particularly convenient for areas of extreme weather variations, high sediment mobility, and/or large study sites where multi-day terrestrial surveys are vulnerable to capturing evolving topography rather than snapshots (Williams et al., 2011).

Costs associated for the effectively reduced six day survey were estimated at NZ\$11,500 with operation costs estimated at: labor NZ\$900 day^{−1} per person, RTK-GPS (with base, receiver, and repeater) NZ\$550 day^{−1}, camera NZ\$50 day^{−1}, flight NZ\$1100, and initial

PhotoScan purchase NZ\$686 (with educational license, standard license NZ\$4400). However, once the study site was established, and if GCPs were placed in long-term locations with low risk of disturbance, repeat surveys could likely be completed in three days at a cost of NZ\$6500. Compared to a LiDAR (without bathymetric mapping) quote received at NZ\$28,000 for an initial survey, and NZ\$26,000 for repeat surveys, the presented SfM–DMVR, ToPCAT, optical bathymetric mapping workflow was considerably less expensive yet the results presented for the study reach illustrate that this workflow can produce DEMs with comparable resolution, precision, and accuracy. Post-processing costs were not included in the estimate of this workflow since alternative methods (i.e. LiDAR, RTK-GPS survey, or TLS) all have inherent post-processing. Nevertheless, assuming the user has a general

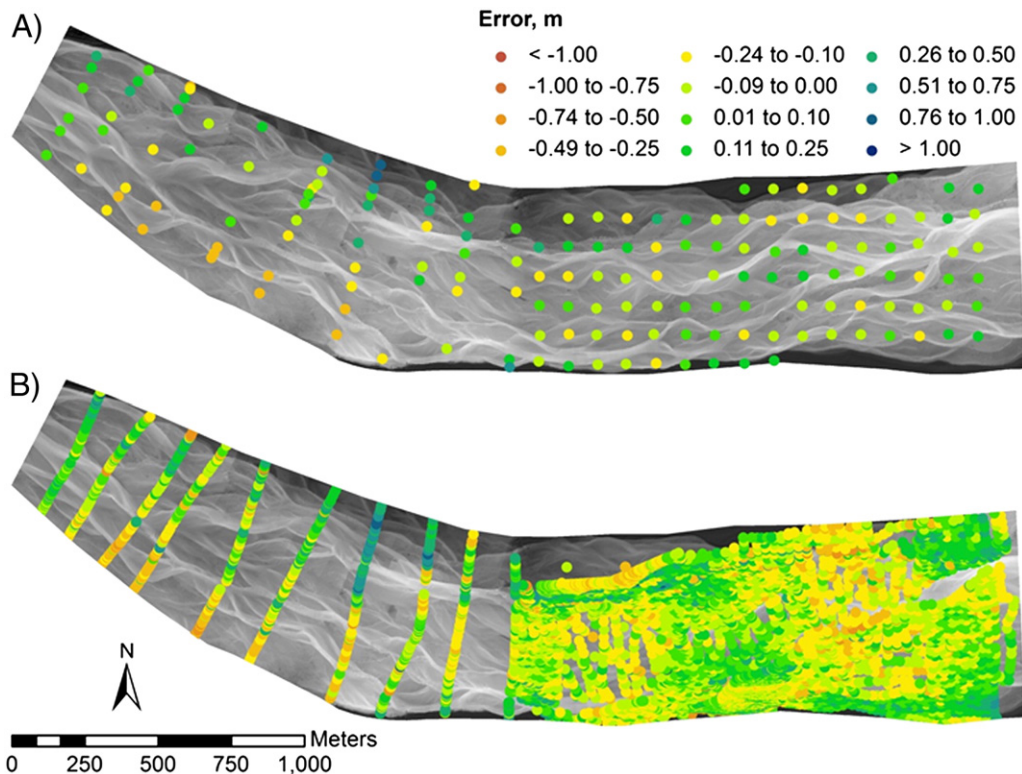


Fig. 12. Optimized transformed full reach spatial distribution and color-coordinated residual z-errors for A) GCPs, and B) all ground truth points.

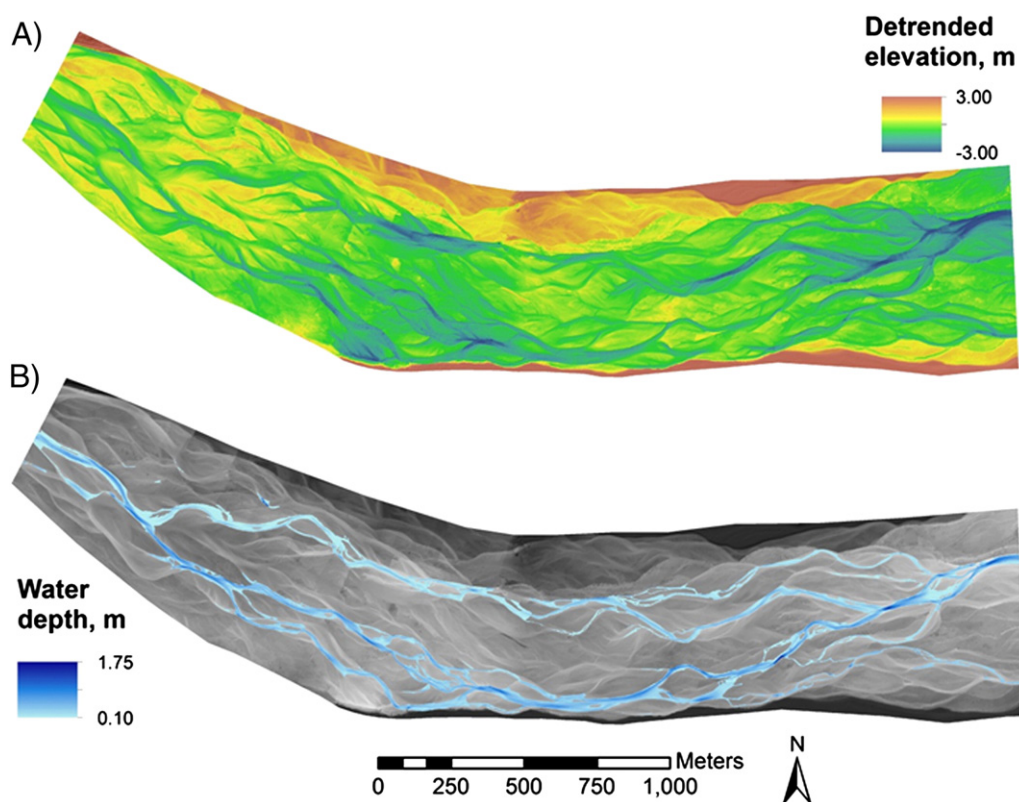


Fig. 13. Full reach A) detrended DEM, and B) bathymetric mapping.

understanding of PhotoScan and ArcGIS raster generation, post-processing the study reach DEM could be completed within one week, with bathymetric mapping requiring the majority of time.

8. Conclusion

A quality assessment of the workflow combination utilizing SfM, ToPCAT point cloud filtering, and optical–empirical bathymetric mapping to produce large scale DEMs has been presented. Comparison between the study reach and extended reach models revealed the study reach's superior performance. With overlapping images and ground control quality of the significant difference in model production, these results highlight the importance of extensive and accurate data acquisition. While the study reach highlights the capabilities of the described workflow, the reasonable errors of the extended reach illustrate the potential for this workflow to produce qualitatively convincing DEMs from retrofitted data thus, significantly increasing the topographic detail and research opportunities of pre-existing or limited datasets.

This workflow offers non-expert users the ability to effectively produce DEMs of moderately vegetated fluvial environments without high data acquisition costs or exhaustive field labor; thus, increasing the extent and frequency of surveys. With resolutions of 0.21 m and average vertical surface errors as low as 0.10 m obtained, the achieved topographic detail and quality are fit for the purpose of morphological change detection and hydrodynamic modeling. While the results presented do not compare to the accuracy, precision, or resolution achieved from TLS, other researchers (Doneus et al., 2011) have achieved similar performance with SfM–MVS. Therefore, given that image resolution and program settings utilized in this paper could be improved, it is likely that this workflow can create large scale DEMs at resolution and accuracies that compare with TLS, provided a computer more capable than the one utilized in this paper.

This study also showed that this workflow was capable of modeling a 3.3 km river reach with surface accuracies dependent upon the local photocontrol quality. Based on these results, it is assumed that this

workflow could be applied to larger scale studies given a capable computer. Further, while this study focused on a braided river with moderate floodplain vegetation during dormant conditions, it is reasonable that this workflow could be applied to other river settings with various vegetation conditions. However, as illustrated in this paper, vegetation would be a primary concern with dense vegetation or wooded forests likely causing the greatest challenges. While the study reach had areas of dense willow thickets, the SfM + ToPCAT model and SfM–Veg model were able to penetrate to the ground surface due to leafless canopies. Naturally, this ground penetration will reduce with increasing canopy density during growing seasons as well as in coniferous forests, and thus likely cause greater vegetation noise. Nevertheless, it is possible to penetrate dense vegetation given a high initial point cloud resolution and larger ToPCAT grid size. However, given these undesirable conditions, it would be beneficial to collect high-density ground truthing data in such vegetated areas to provide adequate testing and/or manual elevation calibration if necessary.

Acknowledgments

This research was funded in part by the New Zealand Department of Conservation's Project River Recovery and the University of Canterbury. The authors would like to thank those who helped organize and collect the field data: Murray Hicks, Tim Davies, Chris Woolmore, Paul Bealing, Patrick Kailey, Callum Pithie, and Laura Edmondson.

References

- AgiSoft, 2010. AgiSoft PhotoScan professional edition. Retrieved October 17, 2012 from <http://www.agisoft.ru/products/photoscan/>.
- AgiSoft, 2012. Agisoft PhotoScan User Manual: Professional Edition. Version 0.9.0. Retrieved June 15, 2012 from <http://www.agisoft.ru/products/photoscan/professional/>.
- Baltsavias, E.P., 1999. A comparison between photogrammetry and laser scanning. *ISPRS Journal of Photogrammetry and Remote Sensing* 54, 83–94.
- Beavan, J., Denys, P., Denham, M., Hager, B., Herring, T., Molnar, P., 2010. Distribution of present-day vertical deformation across the Southern Alps, New Zealand, from

- 10 years of GPS data. *Geophysical Research Letters* 37, L16305. <http://dx.doi.org/10.1029/2010GL044165>.
- Brasington, J., Rumsby, B.T., McVey, R.A., 2000. Monitoring and modeling morphological change in a braided gravel-bed river using high resolution GPS-based survey. *Earth Surface Processes and Landforms* 25, 973–990.
- Brasington, J., Langham, J., Rumsby, B., 2003. Methodological sensitivity of morphometric estimates of coarse fluvial sediment transport. *Geomorphology* 53, 299–316.
- Brasington, J., Vericat, D., Rychkov, I., 2012. Modeling river bed morphology, roughness, and surface sedimentology using high resolution terrestrial laser scanning. *Water Resources Research* 48, W11519. <http://dx.doi.org/10.1029/2012WR012223>.
- Carbonneau, P.E., Lane, S.N., Bergeron, B., 2006. Feature based image processing methods applied to bathymetric measurements from airborne remote sensing in fluvial environments. *Earth Surface Processes and Landforms* 31, 1413–1423.
- Chandler, J., 1999. Effective application of automated digital photogrammetry for geomorphological research. *Earth Surface Processes and Landforms* 24, 51–63.
- Charlton, M.E., Large, A.R.G., Fuller, I.C., 2003. Application of airborne LiDAR in river environments: the River Coquet, Northumberland, UK. *Earth Surface Processes and Landforms* 28, 299–306.
- Dandois, J.P., Ellis, E.C., 2013. High spatial resolution three-dimensional mapping of vegetation spectral dynamics using computer vision. *Remote Sensing of Environment* 136, 259–276.
- Doneus, M., Verhoeven, G., Fera, M., Briese, C., Kucera, M., Neubauer, W., 2011. From deposit to point cloud – a study of low cost computer vision approaches for the straightforward documentation of archaeological excavations. Proc. XXIIIrd International CIPA Symposium. Czech Republic, Prague.
- Fonstad, M.A., Marcus, W.A., 2005. Remote sensing of stream depths with hydraulically assisted bathymetry (HAB) models. *Geomorphology* 72, 320–339.
- Fonstad, M.A., Dietrich, J.T., Courville, B.C., Jensen, J.L., Carbonneau, P.E., 2013. Topographic structure from motion: a new development in photogrammetric measurement. *Earth Surface Processes and Landforms* 38, 421–430.
- Griffiths, G.A., 1981. Some suspended sediment yields from South Island catchments, New Zealand. *JAWRA Journal of the American Water Research Association* 17, 662–671.
- Hicks, D.M., Shankar, U., McKerchar, A.L., Basher, L., Lynn, I., Page, M., Jessen, M., 2011. Suspended sediment yields from New Zealand rivers. *Journal of Hydrology* 50, 81–142.
- Hilldale, R.C., Raff, D., 2008. Assessing the ability of airborne LiDAR to map river bathymetry. *Earth Surface Processes and Landforms* 33, 773–783.
- James, M.R., Robson, S., 2012. Straightforward reconstruction of 3D surfaces and topography with a camera: accuracy and geoscience application. *Journal of Geophysical Research – Earth Surface* 117, F03017. <http://dx.doi.org/10.1029/2011JF002289>.
- Kreylos, O., Cowgill, E.S., Oskin, M.E., Gold, P.O., Elliott, A.J., Kellogg, L.H., 2013. Point-Based Computing on Scanned Terrain with LiDAR Viewer. *Geosphere* 9, 546–556.
- Land Information New Zealand, 2002. Crown Pastoral Land Tenure Review: Ben Avon Lease. Conservation Resources Report.
- Lane, S.N., James, T.D., Crowell, M.D., 2000. Application of digital photogrammetry to complex topography for geomorphological research. *The Photogrammetric Record* 16, 793–821.
- Legleiter, C.J., 2012. Remote measurement of river morphology via fusion of LiDAR topography and spectrally-based bathymetry. *Earth Surface Processes and Landforms* 37, 499–518.
- Lowe, D., 2004. Distinctive image features from scale-invariant keypoints. *International Journal of Computer Vision* 60, 91–110 (440).
- Marcus, W.A., Fonstad, M.A., 2008. Optical remote mapping of rivers at sub-meter resolutions and watershed extents. *Earth Surface Processes and Landforms* 33, 4–24.
- Marzloff, I., Poesen, J., 2009. The potential of 3D gully monitoring with GIS using high-resolution aerial photography and a digital photogrammetry system. *Geomorphology* 111, 48–60.
- Pickrill, R.A., Irwin, J., 1986. Circulation and sedimentation in Lake Benmore, New Zealand. *New Zealand Journal of Geology and Geophysics* 29, 83–97.
- Robertson, D.P., Cipolla, R., 2009. Structure from Motion. In: Varga, M. (Ed.), *Practical Image Processing and Computer Vision*. John Wiley, Chichester.
- Rychkov, I., Brasington, J., Vericat, D., 2012. Computational and methodological aspects of terrestrial surface analysis based on point clouds. *Computers and Geosciences* 42, 64–70.
- Semyonov, D., 2011. Algorithms used in Photoscan [Msg 2]. Retrieved May 3. Message posted to www.agisoft.ru/forum/index.php?topic=89.0.
- Trimble, 2012. Datasheet: Trimble R8 GNSS Receiver. Retrieved July 24, 2012 from http://www.trimble.com/trimbler8gnss_ds.asp.
- Verhoeven, G., 2011. Taking computer vision aloft – archaeological three-dimensional reconstructions from aerial photographs with photoscan. *Archaeological Prospection* 18, 67–73.
- Verhoeven, G., Doneus, M., Briese, C., Vermeulen, F., 2012. Mapping by matching: a computer vision-based approach to fast and accurate georeferencing of archaeological aerial photographs. *Journal of Archaeological Science* 39, 2060–2070.
- Wedding, L.M., Friedlander, A.M., McGranaghan, M., Yost, R.S., Monaco, M.E., 2008. Using bathymetric LiDAR to define nearshore benthic habitat complexity: implications for management of reef fish assemblages in Hawaii. *Remote Sensing of Environment* 112, 4159–4165.
- Westaway, R.M., Lane, S.N., Hicks, D.M., 2003. Remote survey of large-scale braided, gravel-bed rivers using digital photogrammetry and image analysis. *International Journal of Remote Sensing* 24, 795–815.
- Westoby, M.J., Brasington, J., Glasser, N.F., Hambrey, M.J., Reynolds, J.M., 2012. 'Structure-from-Motion' photogrammetry: a low-cost, effective tool for geoscience applications. *Geomorphology* 179, 300–314.
- Wheaton, J., 2012. Geomorphic change detection. Retrieved March 17, 2012 from gdc.joewheaton.org.
- Wheaton, J.M., Brasington, J., Darby, S.E., Sear, D., 2010. Accounting for uncertainty in DEMs from repeat topographic surveys: improved sediment budgets. *Earth Surface Processes and Landforms* 35, 136–156.
- Wheaton, J.M., Brasington, J., Darby, S.E., Kasprak, A., Sear, D., Vericat, D., 2013. Morphodynamic signatures of braiding mechanisms as expressed through change in sediment storage in a gravel-bed river. *Journal of Geophysical Research – Earth Surface* 118, 759–779.
- Williams, R., Brasington, J., Vericat, D., Hicks, D.M., Labrosse, F., Neal, M., 2011. Monitoring braided river change using terrestrial laser scanning and optical bathymetric mapping. In: Smith, M.J., Paron, P., Griffiths, J.S. (Eds.), *Geomorphological Mapping: Methods and Applications*. Elsevier, Oxford, UK, pp. 507–532.
- Williams, R., Brasington, J., Hicks, D.M., Measures, R., Rennie, C.D., Vericat, D., 2013a. Hydraulic validation of two-dimensional simulations of braided river flow with spatially continuous aDcp data. *Water Resources Research* 49, 5183–5205.
- Williams, R.D., Brasington, J., Vericat, D., Hicks, D.M., 2013b. Hyperscale terrain modelling of braided rivers: fusing mobile terrestrial laser scanning and optical bathymetric mapping. *Earth Surface Processes and Landforms*. <http://dx.doi.org/10.1002/esp.3437>.
- Winterbottom, S.J., Gilvear, D.J., 1997. Quantification of channel bed morphology in gravel-bed rivers using airborne multispectral imagery and aerial photography. *Regulated Rivers: Research and Management* 13, 489–499.